Magnetic Resonance Imaging of the Filtration Process

Conrad J. Dirckx, Simon A. Clark, and Laurance D. Hall
Herchel Smith Laboratory for Medicinal Chemistry, University of Cambridge School for Clinical Medicine, Cambridge, CB2 2PZ, U.K.

Brian Antalek, Joe Tooma, J. Michael Hewitt, and Ken Kawaoka
Eastman Kodak Company, Research Laboratories, Rochester, NY 14650

This article demonstrates that 3-D magnetic resonance imaging (MRI) provides sufficient spatial resolution to visualize accurately the internal architecture of a 10-in. cartridge filter and housing. A paramagnetic material (< 5-μm iron-oxide particles) used as the contaminant, together with a gradient-echo imaging sequence, enables location of the areas on the filter surface where the particles are deposited, even at the earliest stages of blocking. The magnetic susceptibility contrast mechanism of MR imaging sequence and particulate matter produces a far larger volume reduction in MR signal than that generated by the actual displacement of fluid by the particles. Using this spatial amplification effect, the temporal performance of the filter was studied by imaging the deposition of 3.75 g of the particulate material at ten incremental stages of blocking. Blocking is heterogeneous initially, both longitudinally along the filter length and radially across the transverse sections, and continues to be heavier in the areas of initially greater deposition as more material is entrapped. The correlation between the areas of heavy blocking and the internal support structure of the filter cartridge is discussed, since those regions appear to be strongly related to the cartridge body design. In a separate set of experiments, the 3-D flow field of a Newtonian fluid through the filter system was measured for an unblocked filter. These measurements also show some correlation between the spatial heterogeneity of particulate deposition and the heterogeneous flow paths of liquid through the filter.

Introduction

The removal of particulate matter from fluid suspensions is of fundamental importance to a wide range of industries, including fuel (automobiles, central heating boilers); chemical and pharmaceutical manufacturing and analysis; domestic and industrial water customers and the water treatment industry. The diversity of these applications has resulted in a wide variety of filter design, ranging from the simplest filter papers used in coffee machines, to sophisticated porous micro-membrane filters used in kidney dialysis units. Conventionally, there are two distinct classifications of filtration mechanisms: accumulation of the solid on the filter medium, or retention of the solid within a deep porous bed. The present study has concentrated on the mechanisms of surface filtration, although the same techniques could also be adopted for retentive filter studies.

Although there are a number of analytical methods which can be used to monitor the efficiency with which a particular filter operates, for example, the measurement of pressure change across the filter medium, in practice the industrial use and design of filters tends to be based on experience. Given the substantial capital and environmental running costs associated with industrial filtration, it would clearly be of great interest and potential importance to have direct, real-

Correspondence concerning this article should be addressed to L. D. Hall.

time visualization of the filtration process. Ideally, such measurements should provide quantitative, as well as qualitative, data on the temporal and spatial variations of the filtration process. The principle purpose of this article is to demonstrate that this objective can readily be achieved using Magnetic Resonance Imaging (MRI). Although MRI is primarily used in a clinical setting for obtaining high resolution images of internal structures of the human body, it is also commonly used to visualize the location of water in a wide range of porous media such as rock or food. In addition, MRI is uniquely capable of measuring in three dimensions the flow velocity field of fluids such as water or oil as they move through opaque media. Consequently, it is possible to quantitate in three dimensions the flow velocity field of a fluid as it circulates inside a filter housing and passes through the filter membrane and to demonstrate that it is the spatial heterogeneity of this flow which results in nonuniform blocking of the filter.

Previous MRI studies in the field of filtration have included its use to: measure the flow field in hollow fiber membranes (Heath et al., 1990; Yao et al., 1995); follow the porosity of a filter cake in a test system designed to model the filtration and expression of slurry (Laheij et al., 1996); and monitor the invasion and clogging of clay in porous rock under fluid pressure (Fordham et al., 1991).

Since the present study makes use of a number of MRI techniques which will be unfamiliar to those involved in filtration, it is appropriate to provide here a brief introduction to them. MRI exploits the phenomenon of nuclear magnetic resonance (NMR), which was originally demonstrated by Bloch and Purcell in 1946 and is the basis of NMR spectroscopy (Bloch et al., 1946; Purcell et al., 1946). The first MRI experiment was performed by Lauterbur (1973) and, in the subsequent 25 years, the field of MRI has grown enormously both in terms of improvements in image quality and speed of acquisition, but also in the range of possible imaging experiments and applications. Its principle role is as a powerful, medical diagnostic imaging modality, providing totally noninvasive anatomical medical images of astonishingly high resolution and contrast (Gadian, 1982; Morris, 1986). However, MRI has also proved to be an extremely flexible tool for visualizing and quantitatively measuring dynamic physical phenomena such as fluid flow and diffusion in both organic and nonorganic systems (Conturo et al., 1995; Kose et al., 1985; Price et al., 1985). For a complete introduction to the subject, the following texts provide an excellent general guide to the theory and practice of MRI (Callaghan, 1991; Ernst et al., 1987); the review article by Gladden (1994) provides a comprehensive survey of the use of MRI in chemical engineering applications.

In conventional MRI, image-intensity and contrast between different elements of the sample is provided by the density of water protons in a given location together with their intrinsic relaxation. Those relaxation properties are a function of the local molecular environment in which the nuclei are found, and their relative contribution to image contrast can either be enhanced or suppressed depending on the parameters of the imaging experiment. In addition, the MR signal obtained from protons at a given location may be reduced by the presence of neighboring material which has an intrinsic magnetic susceptibility greatly different from that of the magnetic susceptibility of the molecules containing these protons. It is usual to attempt to minimize this effect as much as possible as it can result in unwanted image artefacts and loss of MR signal. However, in the series of experiments described in this article, novel use is made of the magnetic susceptibility difference between the iron species in the particles and water to provide a high level of image contrast between the deposited particles, the filter medium, and the surrounding water. The iron (III) oxide used as the particulate matter to be filtered has very high magnetic susceptibility relative to that of water, and its presence can be detected due to a suppression of the signal from the neighboring volume of water. The use of this technique gives rise to a *spatial amplification* effect in which the volume of surrounding water from which the signal has been suppressed is considerably larger than the actual volume occupied by the deposited matter.

Experimental Methods

All MRI measurements were made using an Oxford Instruments 100 cm bore, 2 Tesla superconducting solenoid magnet connected to a modified Bruker MSL-400 console operating under TOMIKON software (Bruker Medzin Technik GmbH, Karlsruhe, Germany). The magnetic field gradient set was designed and built in-house and its wiring configuration was automatically generated using software based on a genetic algorithm (Fisher, 1996). The set used for horizontal experiments was mounted on a cylindrical plastic former (24 cm internal diameter, 45 cm long), which was capable of producing a maximum field gradient strength of 1.77 mT/cm. A quadrature birdcage R.F. probe of 16 cm ID (built in-house) was used for the experiments. All MR data were transferred from the Bruker Aspect 3000 computer to a network of UNIX workstations by means of in-house hardware and software. 2-D image visualization and analysis was performed using in-house software based on the CAMRES libraries (CaMReS, Dr. N. J. Herrod). 3-D images were rendered on a Silicon Graphics workstation using the *volren* volume rendering software.

Filter details

The filters used were 10 in. PALL fluted paper cartridge filters, housed in a PALL polypropylene casing (Pall Trinity Micro Corp., Cortland, NY) and rated with a pore size ranging from 7 to 9 μm. The filters are cylindrical in shape with the pleated folds of the filter media held onto a plastic former which contains holes through which the filtrate passes. That fluid passes from the outside of the filter surface to the inside of the filter body leaving the contaminant deposited on the filter surface. The filter and housing is shown in Figure 1. To facilitate repeated measurements, the filter casing was mounted inside a perspex cylinder; this was securely fastened to the inside of the bore of the R.F. probe which was in turn fitted to the inside of the bore of the gradient set.

Particulate matter and filtrate

All static imaging experiments which involved the visualization of blocking were performed using iron (III) oxide par-

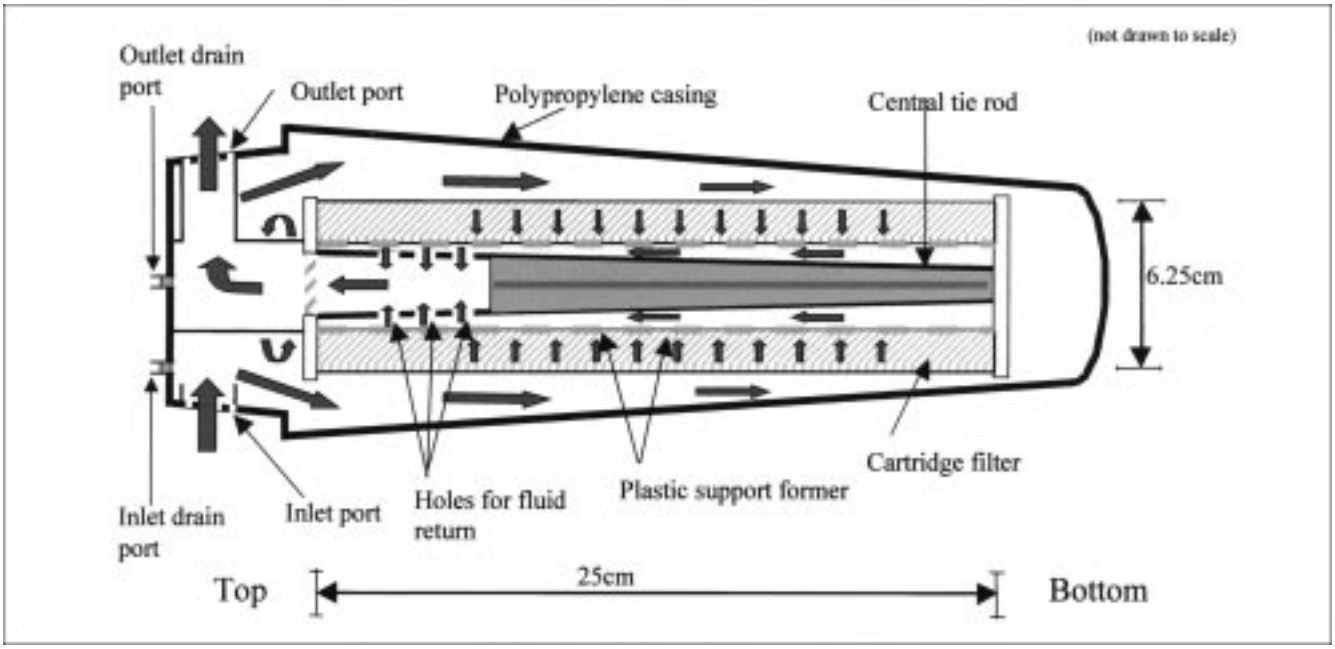

Figure 1. Internal architecture of the filter and its housing.

Arrows indicate the direction of fluid flow through the filter.

ticles of diameter < 5 micron ($+99\%$, cat. no. 31,005-0 Aldrich Chemical Company, Milwaukee, WI). Particle analysis performed at Eastman Kodak, Rochester, NY showed that mean particle diameter of these beads is 2.4 ± 1.08 μm; the median diameter is 2.27 μm and the modal diameter is 2.423 μm.

The challenge solution was 20 mM aqueous copper sulfate which was chosen to reduce the longitudinal (T1) relaxation time constant of water from approximately 2.5 s to approximately 50 ms in order to facilitate faster imaging times.

Details of the flow equipment used

The arrangement of magnetic resonance flow imaging apparatus is shown in Figure 2. An electromagnetically driven gear pump (Integral Series 120 pump, Micropump Inc., Vancouver, WA) was used to provide a constant rate of fluid flow to the filter. The inlet and outlet pressure in the delivery system was continuously monitored during the experiment using pressure monitors. The flow rate was measured gravimetrically at the outlet pipe.

Care was taken to ensure that as much air as possible was expelled from the filter body and, in particular, that there were as few small air bubbles as possible trapped at the filter surface; this is necessary as the air bubbles give rise to susceptibility artefacts which are similar to those of the iron (III) oxide particles. The procedure for eliminating air was to pre-fill the filter housing with clean challenge solution before placing the filter inside the filter housing. Clean fluid was then passed through the filter system from inlet to outlet until no more air bubbles were observed to leave the filter housing, even on agitation. The direction of flow was then reversed and again the clean fluid was passed through the filter system until no more air was observed to leave the filter system.

Details of MR experiments

The MRI experiments were divided into two categories: first, static imaging of the filter with no flow to determine the location of the deposited iron-oxide particles; secondly, dynamic imaging of the fluid flowing through the filter in order to measure the flow velocity field.

For static imaging, two imaging protocols were employed. High-resolution 3-D gradient-echo imaging of the clean filter filled with the challenge solution was employed to show the internal filter architecture. A GEFI imaging sequence (Frahm

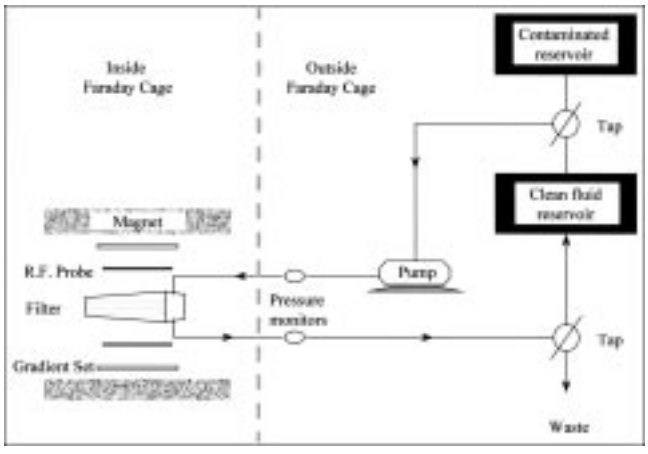

Figure 2. Flow rig used for this study.

et al., 1986) was used to acquire these images in 40 min, using the following MR parameters: TR = 200 ms, TE = 10 ms, flip angle = 45°, nex = 2; the field of view (FOV) was 12×12 ×15 cm with a matrix size of 256×256×64 giving a resolution of 0.47×0.47×2.4 mm. (The lower resolution was along the length of the filter.)

The location of the deposited iron oxide particles and the progress of deposition over time was monitored via a series of 10, fast 3-D MR scans. A spoiled GRASS (SPGR) imaging sequence (Zur et al., 1991) was used to acquire each of these images in 10 min, using the following MR parameters: TR = 30 ms, TE = 7.5 ms, flip angle = 45°, nex = 1, the field of view (FOV) was 12×12×24 cm with a matrix size of 256×256×64 giving a resolution of 0.47×0.47×3.75 mm. (Again the lower resolution was along the filter axis.)

Initially, the filter system was filled with clean challenge solution and placed inside the MR imaging hardware as shown in Figure 2. The ''clean'' reservoir was filled with clean challenge solution and the ''contaminated'' reservoir was filled with challenge solution mixed with the iron (III) oxide powder at a concentration of 0.0625 g/L. Complete mixing was achieved by continuously stirring the suspension with an overhead stirrer.

The first 3-D MR scan was performed as specified above. The flow was then turned on, and, for 90 s, fluid from the contaminated reservoir was allowed to flow through the filter and then to the waste collection vessel; the flow rate was 4.5 L/s. After 90 s, the flow was then switched to the clean fluid reservoir and all contaminated fluid was flushed through the filter for one minute. The output was then redirected towards the clean reservoir for recirculation and the flow rate was measured gravimetrically at the outlet pipe, and inlet and outlet pressures to the filter were noted. The flow was then stopped and the second 3-D MR scan was acquired using the same imaging protocol as before.

When that scan had been acquired, the flow from the contaminated reservoir was restarted for another period of 90 s and the blocking/imaging cycle as described above was repeated; that is, after the 90 s of contaminated fluid flow, the flow was switched to the clean fluid reservoir for 60 s, the pressures and flow rate were measured, the flow was stopped, and a 3-D MR scan was acquired.

A total of 10 MR scans were acquired, and, throughout the experiment, the flow rate remained constant at 4.5 L/min, and inlet/outlet pressures remained constant at 270 mBar and 90 mBar, respectively. The concentration of iron (III) oxide particles in the contaminated reservoir was 0.0622 g/L and, therefore, each period of 90 s of contaminated fluid passing through the filter led to 0.42 g of iron (III) oxide particles being presented to the filter.

During the dynamic imaging, flow of clean challenge solution through the filter system was kept constant at a rate of 4.5 L/min. A 2-D multislice flow-encoding imaging sequence (low angle motion encoding or LAME) was used with the following MR parameters: TR = 1,500 ms, TE = 12.1 ms, flip angle = 30°, nex = 1; the field of view (FOV) was 12 cm^2 using a 3.33 mm slice thickness with a matrix size of 256×256 giving a resolution of 0.47×0.47×3.75 mm and a total of 45 orthogonal slices were acquired. 3 q values were used to encode velocities in each of the three orthogonal directions (x, y, and z), leading to the acquisition of seven datasets; the values of δ and Δ used were 5 ms and 6 ms, respectively. The total time required to acquire all datasets was 50 min.

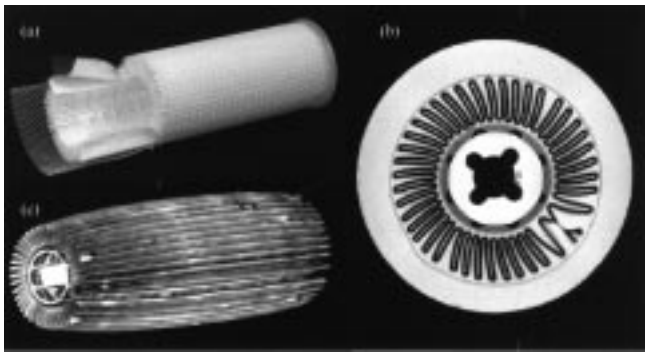

Figure 3. (a) Clean filter, partially cut away to reveal internal support structure; (b) 2-D image of a 5-mm transverse slice through the clean filter in the housing; (c) 3-D rendered MR image of a 12-cm section of a clean filter.

The fine gray line in (a) surrounding the filter is the plastic mesh which surrounds the filter surface. The pleated filter surface, internal filter structure and central support rod are all clearly shown. MR acquisition parameters are listed in the text.

Results and Discussion

2-D and 3-D-rendered MR images of the filter as held inside the filter body are shown in Figure 3; a photograph of the filter (partially cut-away) is shown for comparison. The 3-D MR image is displayed with reverse contrast to that of the acquired MR dataset; that is, those parts of the filter and housing from which there is no MR signal are rendered as solid objects (bright white), whereas all signal from the surrounding fluid has been inverted so as to render it transparent. The pleated structure of the filter is clearly shown together with the plastic former on which the filter material is mounted and the central rod that secures the whole filter element within the housing. The location of the holes in the former is important, as subsequent experiments have implicated this structure in the heterogeneous blocking of the filter.

As stated in the introduction, the spatial amplification effect of using paramagnetic iron (III) oxide particles is to suppress the MR signal from a surrounding volume of water that is much greater than the volume of space occupied by the beads themselves. This gives a much greater apparent thickness of deposited particles than their actual dimensions. This is clearly illustrated in Figure 4 in which a 2-D MR image and a 3-D rendered MR image (partially cut-away) of a blocked filter is shown in comparison with a photograph of the same filter. As with the previous 3-D MR image, reverse contrast was used so that only those voxels which contain no signal are rendered as solid structures. From this image, it is evident that the blocking of the filter is heterogeneous along the length of the filter and the areas of greatest blocking occurs in bands along the length of the filter. This banding can also be seen on the photograph of the filter.

Figure 5 shows the progression of two spatially different transverse sections of the filter as the iron oxide particles

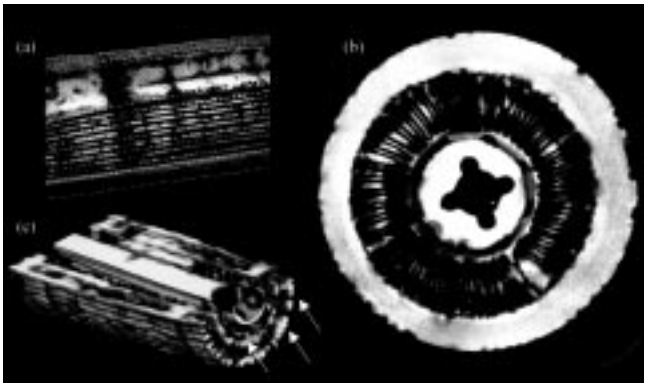

Figure 4. (a) Section of a partially blocked filter showing banding of contaminant deposition; (b) 2-D image of a 5-mm transverse slice through the same blocked filter in the housing; (c) 3-D rendered MR image of a 12-cm section of the same blocked filter.

The accumulation of material at the apex of the filter media can be clearly seen in the 2-D image and is indicated by the arrows in the 3-D image. MR acquisition parameters used are listed in the text.

accumulate over time; the contrast shown is that of the original MR dataset which is such that voxels containing no signal, either due to the lack of fluid or the presence of iron oxide particles, are rendered in black. Both these sections have been chosen as being typical of regions of the filter which have either been lightly blocked or heavily blocked. From these images, it can be seen that initial blockage occurs mainly at the folds of the pleated filter media for both lightly and heavily blocked sections. For lightly blocked regions, this accumulation of the iron oxide continues to be predominately at the folds of the filter media. For the heavily blocked regions, the entire surface of the filter media has become coated with the iron oxide particles. In a subsequent experiment, the direction of flow in the filter was reversed from the inside of the cartridge to the outside. In that experiment, it was noted that the major blocking occurred only on the outer folds of the filter, suggesting that the flow pattern through the filter critically affects the distribution of particles; interestingly, it was noted that banding again occurred along the length of the filter.

The graph in Figure 6 shows the gross progressive blocking of the filter over a 19 cm long section of the filter; each data point represents the mean signal loss between the clean filter and the filter after $t = n$ minutes of flow of the contaminated solution. The location of the holes in the plastic former of the filter cartridge is also shown. The magnitude of this signal loss is qualitatively related to the amount of material deposited on a given transverse section of the filter. The relationship between this mean signal change in a given section and the amount of iron oxide deposited is not linear, as it depends not only on the total amount of paramagnetic material present, but also on its local distribution. As a paramagnetic material accumulates in a given region, the degree of signal loss due to that material in an MR image of that region and the surrounding area initially shows a rapid increase, until most of the signal in that region is destroyed, at which point the increase in signal loss grows much more slowly. This phenomenon is seen in the graph in Figure 6 as a decrease in the rate of signal loss with iron oxide accumulation, as the saturation point of local signal loss is reached.

This graph illustrates several important features about the nature of blocking in this filter. First, as blocking progresses,

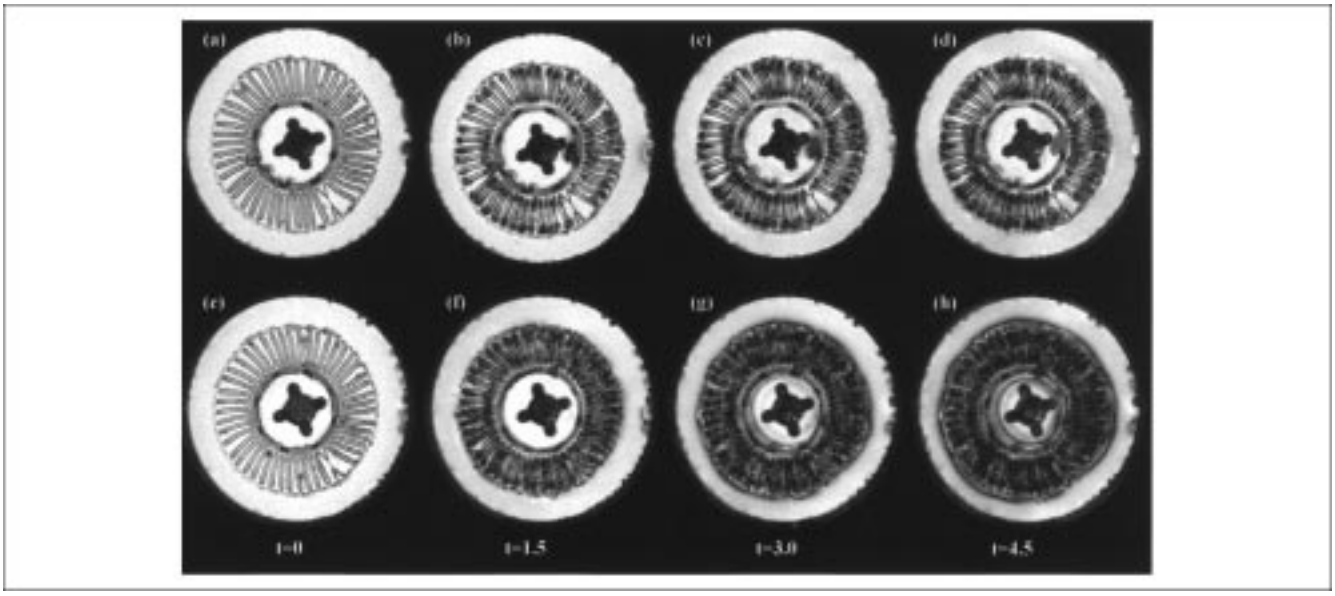

Figure 5. Lightly blocked transverse section of the filter (frames a–d) vs. a heavily blocked transverse section (frames e–h).

Its shows the accumulation of iron oxide particles at four successive time points: $t = 0$, $t = 1.5$, $t = 3$, and $t = 4.5$ min of contaminated fluid flow. The heavily blocked transverse section showed was located 8 cm below the top of the filter, 4 mm below the hole in the central distribution pipe, and the lightly blocked section is located 25 mm below that section.

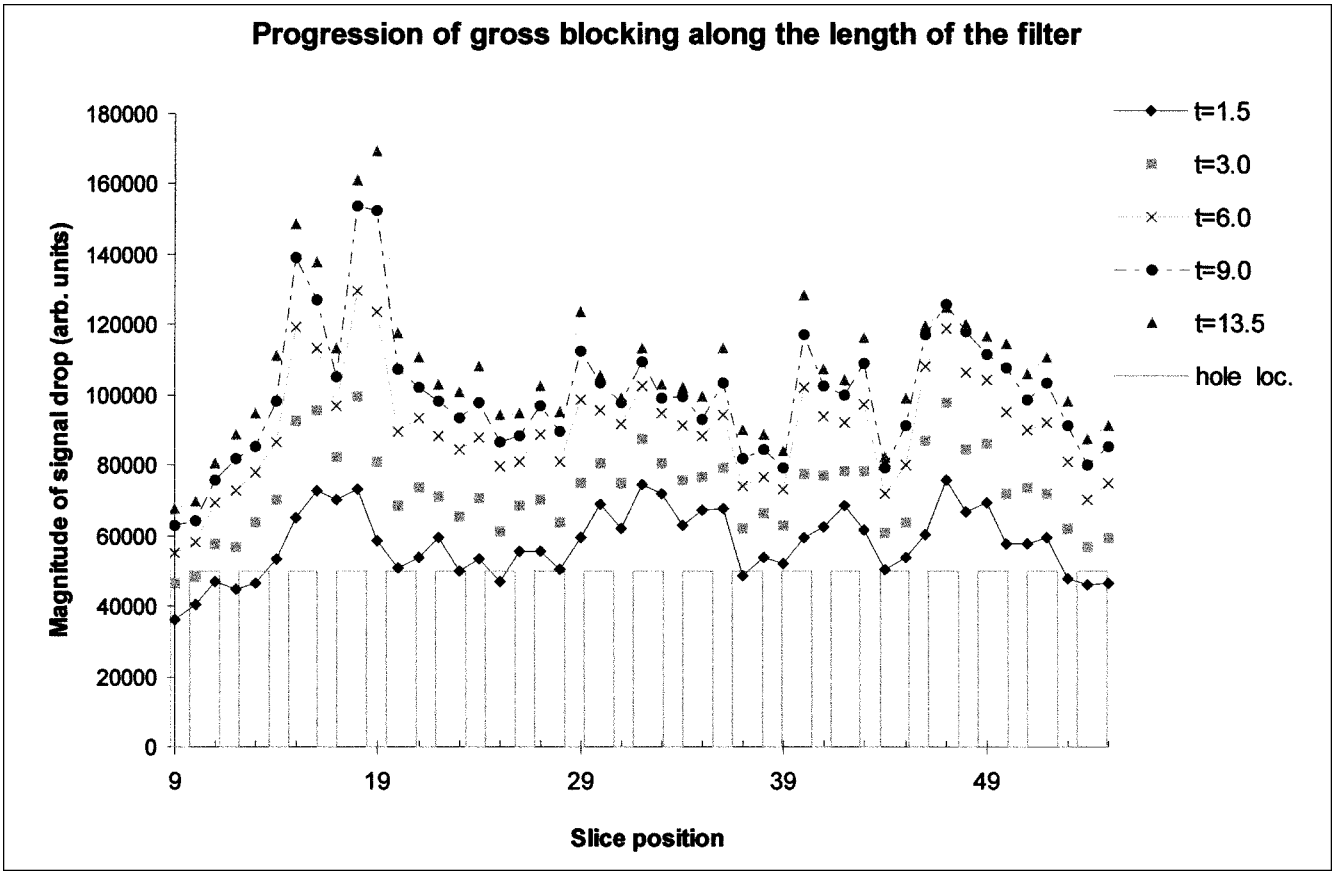

Figure 6. Change in signal intensity over a 19-cm length of the filter is shown above.

Each data point represents the mean signal loss between the clean filter and the filter after $t = n$ minutes of flow of the contaminated solution. The magnitude of this signal loss is qualitatively related to the amount of material deposited on a given slice through the filter. The location of the holes in the plastic former of the cartridge are also shown.

the blocking becomes increasingly heterogeneous along its length, and that those areas of the filter on which the iron (III) oxide particles are initially deposited continue to be the areas on which the iron oxide particles accumulate most heavily. One possible explanation for this may be that the accumulation of particles in a given region initially blocks the larger pores in that region, leading to a reduction of the local rating of the filter media in that area and, hence, the trapping of an increasing number of smaller particles in that region. Some evidence for this hypothesis is given by particle analysis studies of the operation of this type of filter in which the global rating of a filter is commonly observed to decrease over time (Guyon, 1988).

The cause of this banding is likely to be related to the structure of the plastic former which supports the filter media in the cartridge. This structure contains a number of holes which are regularly spaced and through which the fluid flows and returns to the outlet of the filter body. It may be that these are responsible for producing a heterogeneous flow field within the filter which in turn leads to its heterogeneous blocking. The location of these holes within the former are shown on the graph and, from this, we can see that the periodicity of their location is related to the periodicity of variation in the initial blocking. However, this relationship is not simple and it cannot be said that the presence or absence of holes in a given transverse section necessarily leads to light or heavy blocking in that section.

Figure 7 shows the results of the MR velocimetry in one transverse slice for the x, y and z components of velocity within a clean filter. The greatest flow velocities occur longitudinally, along the length of the filter body (z-axis) as fluid flows down the filter body and returns through the central portion of the filter, after having passed through the filter. For the fluid outside the filter, these high longitudinal velocities (z-axis) are confined to the space outside the fine plastic mesh and reach a maximum velocity of 5 cm/s. Inside this mesh, in the space surrounding the filter media, those velocities drop immediately to 1 cm/s and fall away to zero towards the center of the filter. This rapid passage of fluid along the edge of the filter may explain why the progressive blocking study showed that the outermost folds of the filter experience greater blocking than the middle part of the filter media surface as these would be exposed to more contaminant per unit of time than the inner surfaces of the filter media.

The greatest axial velocities (x and y axes) are to be found at the inner folds of the filter as fluid is funnelled down the pleats of the filter and before passing through the filter media. From the pregressive blocking study, it is known that the areas of greatest blocking occur at these inner folds and these higher velocities imply a greater passage of fluid through that

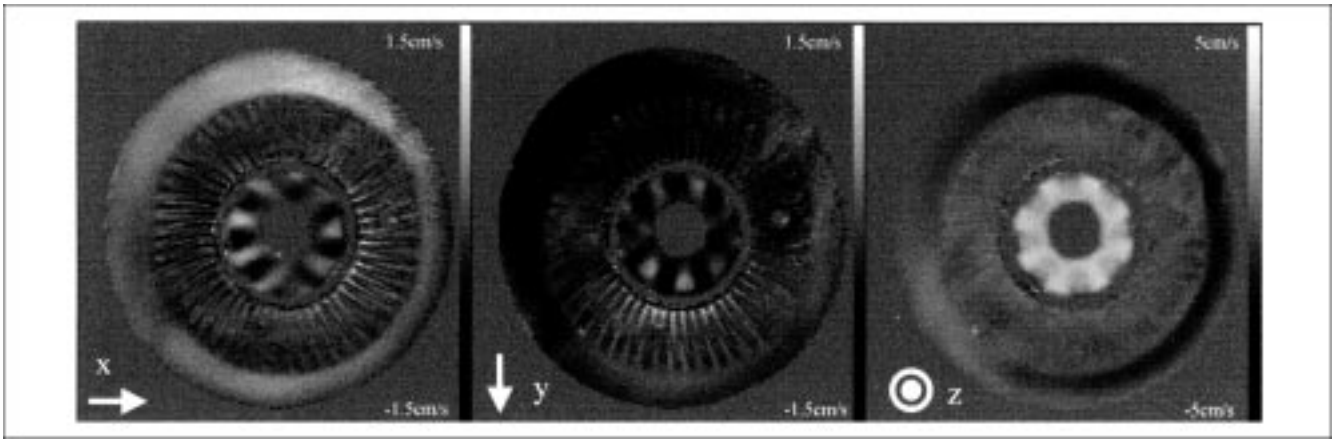

Figure 7. X, Y and Z components of velocity as measured passing through one typical 3.33-mm transverse section of the filter.

Note that the z component of velocity, aligned along the center of the filter, is much greater than the x and y components along the central return space and around the outer perimeter of the filter. This section is located 6 cm from the bottom of the filter. The MR parameters used are listed in the text.

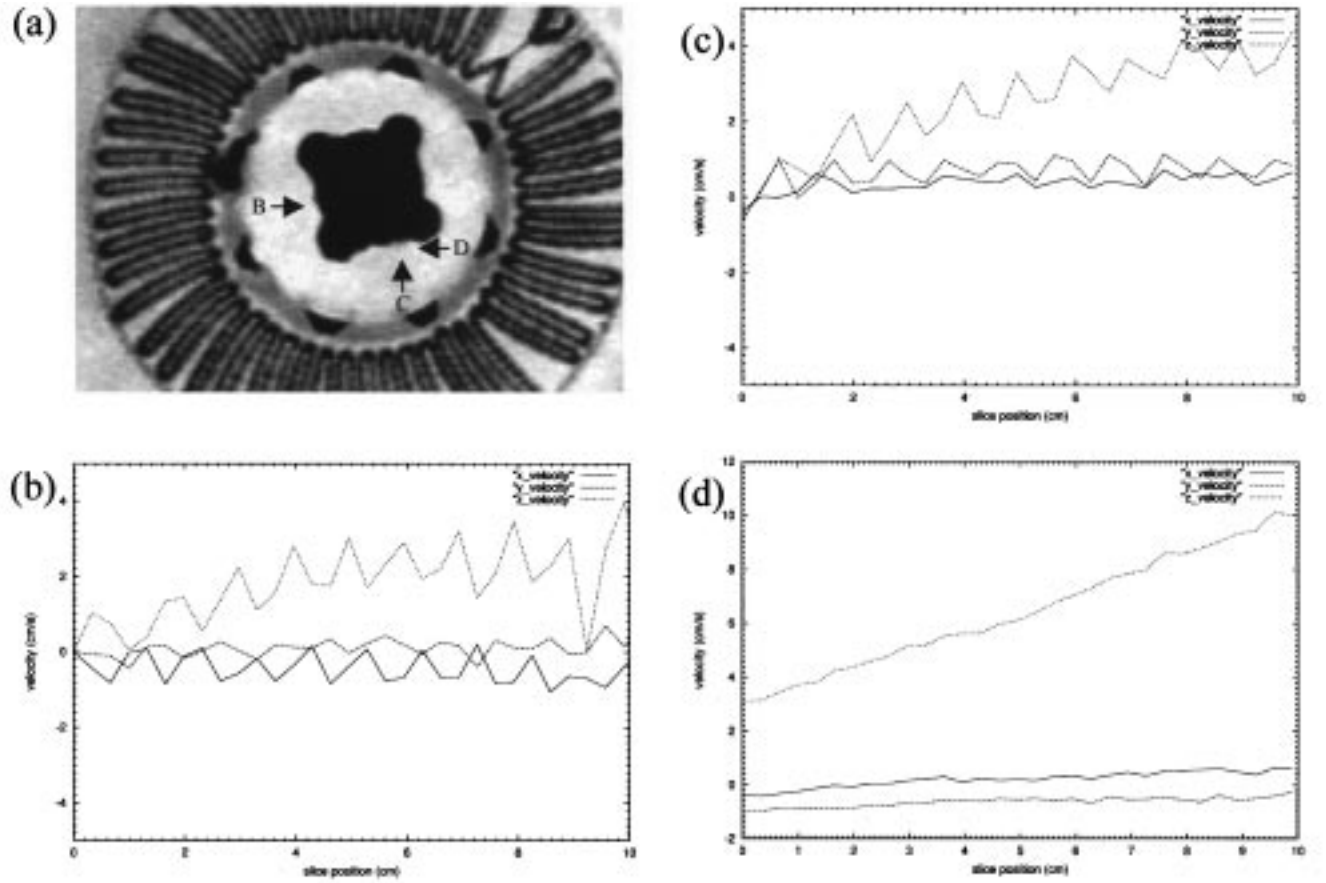

Figure 8. Longitudinal velocity measurements over a 10-cm length of the filter at three different points.

The location of each point is indicated in (a), and, for each point (b, c, and d), a graph is given showing the measured x, y, and z velocity components. Graph (b) shows a point at which the x and z components of velocity oscillate according to whether the axial position is adjacent to a hole in the support structure or not. The y component of velocity is close to zero and is stable along that length of filter. Graph (c) shows a corresponding point, equidistant from the central rod and rotated through 90° about the central axis. As would be expected from symmetry, at this point, the y and z components of velocity oscillate according to whether the axial position is adjacent to a hole in the support structure or not, and the x component of velocity is stable and close to zero. Graph (d) shows a point at which the flow field is not impinged by the fluid rushing out of the holes, and, at this location, the z component of velocity increases steadily, rising from 3 cm/s to 10 cm/s over 10 cm as the fluid approaches the outlet. The x component of velocity is constant and close to zero, whereas the y component of velocity is constant and negative suggesting the presence of small circular currents running along the edge of the central rod.

portion of the filter media per unit time which would explain this phenomenon. The x and y components of velocity also show very clearly the fluid passing through the holes in the former into the central section of the filter. There are circular currents found in this central region which may be formed as the fluid spurts through the holes, hits the central support rod, and is then deflected back away from the center of the filter.

Figure 8 shows the longitudinal velocity measurements over a 10 cm length of the filter at three different points within the central return space of the filter, the locations of these points are shown in Figure 8a. The two points (b) and (c) were chosen as to be representative of areas of fluid flow which were affected by the influx of fluid passing through the holes in the plastic former of the filter cartridge. Graph (b) shows a point at which the x and z components of velocity oscillate according to whether the axial position is adjacent to a hole in the support structure or not; the y component of velocity is close to zero and is stable along that length of filter. Graph (c) shows a corresponding point, equidistant from the central rod and rotated through 90° about the central axis. As would be expected from symmetry, at this point, the y and z components of velocity oscillate according to whether the axial position is adjacent to a hole in the support structure, or not, and the x component of velocity is stable and close to zero. Further analysis of the fluid velocities around this central pipe shows that the passage of fluid through these holes is symmetric and that the velocities do not significantly increase towards the fluid outlet suggesting that the distribution of fluid flow along the length of the filter is broadly homogeneous. Further evidence of this gross homogeneity of image flow along the length of the filter is given by Figure 8d, which shows the x, y, and z components of velocity for a point (d) at which the flow field is not impinged by the fluid rushing out of the holes. At this location, the z component of velocity increases steadily at a rate of increase of 0.7 cm/s/cm as the fluid approaches the outlet. This increase in velocity is due to the steady accumulation of fluid in this central return space towards the top of the filter and also partly due to the tapering of the central tie rod which decreases the available volume of this central space towards the top of the filter. Furthermore, there is a small negative y component of velocity at this point which remains constant along the length of the filter; this is indicative of small circular currents which can be seen in Figure 7c and run along the entire length of the filter.

Conclusions

This work has demonstrated that MRI provides a nondestructive means for studying filtration problems on the same physical scale as is used in real industrial applications. Thus, it is feasible on a routine basis to visualize and measure the internal structures in three dimensions of a filter filled with aqueous medium, provided that it is substantially free of ferrous material. Direct visualization of the contaminant is frequently feasible. However, if it is not, a range of substances are readily available which can easily be detected by their influence on the MR responses of the water surrounding the filter. In the case of the cartridge filter studied in this work, a combination of 3-D-gradient echo MRI in conjunction with paramagnetic iron (III) oxide particles enabled the spatial heterogeneity of blocking to be visualized at a spatial resolution of $0.47 \times 0.47 \times 3.75$ mm.

Using a series of 3-D scans, it is also feasible to study the longitudinal progression of filtration. This present study employed a protocol in which the location of the particles is scanned after every 1.5 min of the flow of a fluid contaminated at a concentration of 0.062 g/L where each scan takes 8 min to acquire. This clearly demonstrated for filtration of micron-sized particles that there was substantial heterogeneity of filter blocking, and this may be spatially related to the internal architecture of the filter support structure, and of the filter cartridge itself. Although the spatial resolution was not high enough to enable those features to be directly correlated with the 3-D flow field of the liquid as it passed through the filter, it is clear that the two are related. Perhaps, the most important finding is the observation that most of the filtered particles are deposited on the apexes of the folded structures in bands related to the region of maximal fluid flow. This suggests that some of the basic concepts of filter design based on maximization of the total area of the filter surface may need to be reconsidered if the resultant folding produces regions of flow stagnation which are unavailable for effective filtration.

It is clear that this study presents at least as many opportunities as problems solved. In particular there is now a pressing need to combine on a directly compatible basis data from MRI measurements with that from all the other methods currently used for studies of filtration, such as assays of particle retention. Ideally, those MRI studies should be made with higher spatial resolution so that it is feasible to correlate spatial blocking with liquid flow. It may be that such studies will shed further insight into fundamental design problems of this well-known class of filter such as the fluid flow inside the filter structures and the effect of the filter pleating and packaging on the overall filtration efficiency. It would also be appropriate in the future to study the filtration of deformable particles; fortunately, the concept of spatial amplification, illustrated for the first time in the present study, is readily extendable to many such particles.

Acknowledgments

We wish to thank Edwin J. Voll and Gary L. Slater for the particle analysis. This work was funded by the Herchel Smith Endowment with support from the Eastman Kodak Company.

Literature Cited

Bloch, F., W. W. Hansen, and M. Packard, ''Nuclear Induction,'' *Phys. Rev.*, **69**, 37 (1946).

Callaghan, P. T., *Principles of Nuclear Magnetic Resonance Microscopy*, Clarendon Press, Oxford (1991).

Conturo, T. E., R. C. McKinstry, J. A. Aronovitz, and J. J. Neil, ''Diffusion MRI: Precision, Accuracy, and Flow Effects,'' *NMR Biomed.*, **8**, 307 (1995).

Ernst, R. R., G. Bodenhausen, and A. Wokaun, *Principles of Nuclear Magnetic Resonance in One and Two Dimensions*, Clarendon Press, Oxford (1987).

Fisher, B. J., ''Design of Gradient Coils for MRI by Genetic Algorithms,'' PhD Thesis, Cambridge University, Cambridge (1996).

Fordham, E. J., T. P. L. Roberts, T. A. Carpenter, and L. D. Hall, ''Dynamic NMR Imaging of Rapid Depth Filtration of Clay in Porous-Media,'' *AIChE J.*, **37**, 1900 (1991).

Frahm, J., A. Haase, and D. Matthaei, ''Rapid Three-Dimensional MR Imaging Using the FLASH Technique,'' *J. Comput. Assist. Tomogr*., **10**, 363 (1986).
Gadian, B., *Nuclear Magnetic Resonance and Its Applications to Living Systems*, Clarendon Press, Oxford (1982).
Gladden, L. F., ''Nuclear-Magnetic-Resonance in Chemical-Engineering-Principles and Applications,'' *Chem. Eng. Sci*., **49**, 3339 (1994).
Guyon, E., *Disorder and Mixing*, Kluwer Academic Publishers (1988).
Heath, C. A., G. Belfort, B. E. Hammer, S. D. Mirer, and J. M. Pimbley, ''Magnetic-Resonance-Imaging and Modeling of Flow in Hollow-Fiber Bioreactors,'' *AIChE J*., **36**, 547 (1990).
Kose, K., K. Satoh, T. Inouye, and H. Yasuoka, ''NMR Flow Imaging,'' *J. of the Physical Soc. of Japan*, **54**, 81 (1985).
Laheij, E. J., P. Kerkhof, K. Kopinga, and L. Pel, ''Determining Porosity Profiles During Filtration and Expression of Sewage-Sludge by NMR Imaging,'' *AIChE J*., **42**, 953 (1996).
Lauterbur, P. C., ''Image Formation by Induced Local Interaction: Examples Employing Nuclear Magnetic Resonance,'' *Nature*, **242**, 190 (1973).
Morris, P. G., *Nuclear Magnetic Resonance in Medicine and Biology*, Clarendon Press, Oxford (1986).
Price, R. R., D. R. Pickens, G. Holburn, J. A. Patton, G. J. Wehr, J. Craig, C. L. Partain, and A. E. James, ''NMR Flow Velocity Imaging,'' *Medical Physics*, **12**, 517 (1985).
Purcell, E. U., H. C. Torrey, and R. Pound, ''Resonance Absorption by Nuclear Magnetic Moments in a Solid,'' *Phys. Rev*., **69**, 127 (1946).
Yao, S., M. Costello, A. G. Fane, and J. M. Pope, ''Noninvasive Observation of Flow Profiles and Polarization Layers in Hollow-Fiber Membrane Filtration Modules Using NMR Microimaging,'' *J. of Memb. Sci*., **99**, 207 (1995).
Zur, Y., M. L. Wood, and L. J. Neuringer, ''Spoiling of Transverse Magnetization in Steady-State Sequences,'' *Magn. Reson. Med*., **21**, 251 (1991).

Manuscript received Dec. 28, 1998, and revision received June 23, 1999.